

Research Article

Open Access



Electrocatalytic CO₂ reduction to CO enabled by Ni-N_x high activity sites formed by three-dimensional porous foams

Anqi Wei^{1,*}, Yang Xu^{1,#}, Jiangfang Wang¹, Lei Shi¹, Chong Wang^{1,*}, Yingjie Wu^{2,*} , Song Liu^{1,*}

¹College of Chemistry, Chemical Engineering and Resource Utilization, Northeast Forestry University, Harbin 150040, Heilongjiang, China.

²School of Medicine and Health, Harbin Institute of Technology, Harbin 150001, Heilongjiang, China.

#Authors contributed equally.

*Correspondence to: Prof. Dr. Song Liu and Prof. Dr. Chong Wang, College of Chemistry, Chemical Engineering and Resource Utilization, Northeast Forestry University, No. 26 Hexing Road, Xiangfang District, Harbin 150040, Heilongjiang, China. E-mail: carlosliu@nefu.edu.cn, wangchong@nefu.edu.cn; Prof. Dr. Yingjie Wu, School of Medicine and Health, Harbin Institute of Technology, No. 92 Xidazhi Street, Nangang District, Harbin 150001, Heilongjiang, China. E-mail: wuyingjie@hit.edu.cn

How to cite this article: Wei, A.; Xu, Y.; Wang, J.; Shi, L.; Wang, C.; Wu, Y.; Liu, S. Electrocatalytic CO₂ reduction to CO enabled by Ni-N_x high activity sites formed by three-dimensional porous foams. *Chem. Synth.* 2025, 5, 81. <https://dx.doi.org/10.20517/cs.2024.205>

Received: 28 Dec 2024 **First Decision:** 22 Apr 2025 **Revised:** 20 May 2025 **Accepted:** 5 Jun 2025 **Published:** 22 Oct 2025

Academic Editor: Teng Ben **Copy Editor:** Xing-Yue Zhang **Production Editor:** Xing-Yue Zhang

Abstract

Single-atom catalysts (SACs) are widely used in carbon dioxide reduction reaction (CO₂RR) due to their distinctive electronic configuration and coordination environment. However, designing catalysts with porous structures that provide more active sites is a challenge in practice. Herein, we utilized the porous network structure of melamine foam (MF) and high temperature calcination to increase the number of nickel atoms to promote the formation of Ni-N_x active sites, resulting in nitrogen-coordinated nickel SACs with high catalytic activity. The X-ray photoelectron spectroscopy test demonstrates that the optimal calcination temperature of 900 °C can achieve a Ni-N_x site content of 9.47 at.%, which is significantly higher than that of other temperature conditions. This confirms that the calcination temperature has a decisive regulatory effect on the nitrogen-doped configuration and the formation of active sites. Furthermore, MF facilitated efficient electron transfer, resulting in improved catalytic performance. The Faradaic efficiency of CO (FE_{CO}) could reach 91% at -0.66 V vs. reversible hydrogen electrode. *In situ* Infrared Spectroscopy for real-time monitoring has demonstrated a linear relationship between Ni-N_x and the reaction intermediate *CO content, indicating that an elevated Ni-N_x content may facilitate the generation of more active sites and expedite the kinetic process of CO₂RR. The density functional theory calculations reveal that the Ni-N₂ coordination in the Ni-N_x surface is responsible for the superior catalytic activity of CO₂RR due to the



© The Author(s) 2025. **Open Access** This article is licensed under a Creative Commons Attribution 4.0 International License (<https://creativecommons.org/licenses/by/4.0/>), which permits unrestricted use, sharing, adaptation, distribution and reproduction in any medium or format, for any purpose, even commercially, as long as you give appropriate credit to the original author(s) and the source, provide a link to the Creative Commons license, and indicate if changes were made.



moderate adsorption strength of $^*\text{COOH}$ with less negative U_L (-0.87 V). This experiment provides an innovative way to increase the active site content of SACs in CO_2RR .

Keywords: CO_2 electroreduction, CO production, single-atom catalysts, reaction mechanism

INTRODUCTION

The utilization of renewable energy sources for the electrocatalytic carbon dioxide reduction reaction (CO_2RR) represents an effective strategy for the sustainable reduction of carbon emissions^[1-3]. Single-atom catalysts (SACs) have demonstrated considerable potential in the field of heterogeneous catalysis, largely due to their distinctive electronic structure and coordination environment^[4,5]. However, CO_2RR exhibits a high kinetic energy barrier and susceptibility to competition with the hydrogen evolution reaction (HER)^[6,7]. Therefore, further design of SACs is still needed to improve the selectivity of CO_2RR .

Metal-nitrogen-carbon (M-N-C) catalysts demonstrate remarkable efficacy in CO_2RR due to their distinctive chemical structure^[8-10]. In comparison with conventional M-N-C materials, M-N-C catalysts with a porous structure exhibit larger specific surface area and an increased number of active sites^[11,12]. Liu *et al.* developed porous carbon carriers, which resulted in a 5-fold increase in active site exposure. This structure was shown to significantly enhance catalytic performance^[13]. Pan *et al.* prepared atomically dispersed M-N-C catalysts with M-N_4 sites using zeolite imidazolium salt skeleton-8 (ZIF-8). The reactivity and catalytic sites of M-N_4 ($\text{M} = \text{Fe}$ or Co) for CO_2 reduction were comprehensively investigated^[14]. Wang *et al.* developed a hybridization method of precursors for the preparation of N-doped porous carbon (NPC). A direct strategy was provided for the rational design of N-doped carbon catalysts with abundant pyridine-N active sites^[15]. However, in the process of forming M-N_x at high temperatures, due to the high migration rate and diffusion rate of metal atoms, it is easy to lead to the formation of metal clusters and the decrease of M-N_x density^[16-19]. Therefore, it is a great challenge to construct a new catalyst with high M-N_x content^[19-22].

Melamine foam (MF) is a highly cross-linked thermosetting organic porous plastic with high mass transfer rates and nitrogen content. The pristine framework of this material possesses a high specific surface area and through pores, which facilitate the diffusion of reactants (carbon dioxide) and desorption of products. Furthermore, the pyrolysis of MF results in the formation of N-doped carbon in the form of graphene-like structures. This process enhances the electrical conductivity of the material and prevents agglomeration into particles by anchoring the nickel single-atom with nitrogen atoms. Herein, in this paper we synthesized Ni SACs by MF pyrolysis. The goal was to form Ni-N_x structures with highly active sites to improve CO_2RR selectivity. The X-ray photoelectron spectroscopy (XPS) test results showed a peak content of Ni-N_x sites in the material (9.47 at.%) at a calcination temperature of 900°C , a value significantly higher than other calcination temperatures. The Faradaic efficiency of CO (FE_{CO}) at -0.66 V vs. reversible hydrogen electrode (RHE) could reach 91% and maintain the basic performance ($\text{FE} > 80\%$) after 35 h of testing. This finding indicated that Ni-N_x was the primary active site of CO_2RR and its content exhibited a direct correlation with catalytic activity. *In situ* infrared spectroscopy (IR) and the density functional theory (DFT) calculations indicated that high-temperature calcination might promote the stable coordination of Ni with N, modulate the electronic state of Ni, and enhance the adsorption of the reaction intermediate $^*\text{CO}$. The results of this experiment demonstrate the potential of a novel approach to the construction of porous catalysts with a binding effect.

EXPERIMENTAL

Materials

Nickel nitrate hexahydrate [$\text{Ni}(\text{NO}_3)_2 \cdot 6\text{H}_2\text{O}$; 98%] from Sigma-Aldrich; potassium bicarbonate (KHCO_3 ; AR) from Shanghai Rhawn Chemical Technology Company; MF from Taobao; liquid nitrogen from Harbin Daoli District Mingying Cryogenic Materials Supply Department; anhydrous ethanol ($\text{C}_2\text{H}_5\text{OH}$; AR) from Tianjin Fuyu Fine Chemical Company; Nafion 117 perfluorinated resin solution (~5% in a mixture of lower aliphatic alcohols and water) from Shanghai Rhawn Chemical Technology Company. The cation exchange membrane employed in this experiment was the Nafion 117 membrane, provided by DuPont. All reagents were provided in a ready-to-use format, requiring no further purification. All solutions were prepared with ultrapure water (specific conductivity $\geq 18.2 \text{ M}\Omega\cdot\text{cm}^{-1}$).

Synthesis of MF-900

MF was impregnated in an equal volume of ultrapure water, frozen with liquid nitrogen and then dried in a vacuum freeze dryer at -80°C for 48 h. It was removed into a tube furnace, sealed, and purged with flowing argon for 30 min to allow the air to escape completely. The tube furnace was heated to 550°C and held for two h, then heated again to 900°C and held for two h. After this, the furnace was allowed to cool naturally to room temperature, after which the sample was removed and designated MF-900.

Synthesis of MF-Ni-800, MF-Ni-900, and MF-Ni-1000

Weigh 0.0012 g of nickel nitrate hexahydrate in a beaker. Subsequently, 4.5 mL of ultrapure water was pipetted into the beaker and stirred with ultrasound until complete dissolution was achieved. Then, 0.05 g of MF was weighed and impregnated in the solution. The material was frozen with liquid nitrogen and subjected to vacuum drying at -80°C for a period of 48 h. Subsequently, the material was removed and placed in a tube furnace, which was sealed and purged with flowing argon gas for 30 min to remove air. The tube furnace was initially heated to 550°C and maintained at this temperature for a period of two h. Subsequently, the material was heated to 800, 900, or $1,000^\circ\text{C}$ and maintained at this temperature for a further two h. The temperature was reduced to ambient levels. The resulting materials were designated MF-Ni-800, MF-Ni-900, and MF-Ni-1000.

Preparation of working electrode

MF was affixed to the working electrode via a special working electrode clamp.

Electrochemical test

The CHI760 workstation from Shanghai Chenhua Instrument Company., Ltd. or the Squidstat Plus electrochemical workstation from Admiral, US, was used for the test.

Principles of electrochemical test

Converting the electrode potential relative to the Ag/AgCl electrode to the electrode potential relative to the standard hydrogen electrode: $E_{\text{RHE}} = E_{\text{Ag/AgCl}} + 0.197 + 0.0592 \times \text{pH}$ where $E_{\text{Ag/AgCl}}$ is the potential at the time of the test (V), and pH is the saturated 0.5 M KHCO_3 solution.

Faradaic efficiency can be calculated by $\text{FE} = ZnF/Q$ where Z denotes the number of electrons transferred (in the reduction of CO_2 to form CO, $Z = 2$), n represents the number of moles of the product (mol), F is Faradaic constant ($96,485 \text{ C/mol}$), and Q is the charge (C).

The Tafel curve is closely related to the kinetic rate and activity, which is calculated as: $\eta = a + b \log j$ where η denotes overpotential (V), a indicates the intercept (V), b denotes the slope (mV/dec), and j signifies the current density (mA/cm^2).

In order to reflect the intrinsic activity of the catalyst, the transition frequency (TOF) is calculated for the catalyst by $\text{TOF} = \frac{j_{\text{product}} \times A/nF}{\omega m/M}$ where j_{product} is the product fraction current density (mA/cm²), A is the electrode geometry (cm²), n is number of electrons to be transferred to produce the product (in the reduction of CO₂ to form CO, $n = 2$), ω is the mass fraction of metal analyzed by ICP-OES (wt%), m is the mass of catalyst at the working electrode (g), and M is the molar mass (g/mol).

Characterization

Calcination of samples using tube furnace of Hefei Kejing Material Technology Co. The vacuum freeze dryer of Ningbo Xinzhi Freeze Drying Equipment Company was used to freeze dry the samples. Scanning electron microscope (SEM; EM-30plus) and high-resolution transmission electron microscope (HRTEM; Talos F200s) were used to observe the morphology of the materials. Spherical aberration corrected transmission electron microscope (AC-TEM; JEOL JEM-ARM200F) was used to determine the presence of single atoms. Spectroscopy was tested by X-ray diffraction (XRD; HZL10004) and Raman spectroscopy (Raman; Thermo Fisher DXR2). N₂ absorption/desorption isotherms were recorded on the Quantachrome station. XPS was performed using a ThermoFisher Scientific ESCALAB 250 Xi+ spectrometer. An Agilent 8890 gas chromatograph was used to test the gaseous products, and FL97Plus was used to test the liquid products. *In situ* IR was detected using a Fourier-transform infrared spectroscopy (FTIR) spectrometer (WQF-530A) with a customized ATR accessory and a liquid nitrogen-cooled Mercury Cadmium Telluride (MCT) detector.

Density functional theory calculations details

The DFT was implemented in the Vienna ab initio simulation package (VASP) to calculate this work^[23,24]. The projector augmented-wave (PAW) was carried out to handle the interactions between the core and the valence electrons^[25,26]. The Perdew-Burke-Ernzerhof (PBE) functional was utilized along with the generalized gradient approximation (GGA) to model the exchange-correlation energy^[27] with the plane-wave cutoff energy of 450 eV. In all calculations, the convergence criterion of energy and force was set to be 10⁻⁶ eV and 0.02 eV·Å⁻¹, respectively. For Brillouin zone sampling, the Γ -centered k -point grid of 3 × 3 × 1 was employed during structure optimization and static self-consistent calculations. The catalytic substrate was modeled by a 5 × 5 graphene supercell, of which the thickness of the vacuum layer was 20 Å in the z -direction to avoid interaction between periodic images. In addition, van der Waals (vdW) interaction was considered by Grimme's DFT-D3 with Becke-Johnson (BJ) damping^[28,29]. To describe the process of electrochemical CO₂RR, the computational hydrogen electrode (CHE) model proposed firstly by Nørskov *et al.* was referred to obtain the free energy profile^[30].

The Gibbs free energy change (ΔG) of each elementary step was defined as $\Delta G = \Delta E + \Delta E_{\text{ZPE}} - T\Delta S + \int C_p dT$ where ΔE and ΔE_{ZPE} represent the change of total and zero-point energy of the system, respectively. The ΔS is the contribution of entropy, and the C_p is heat capacity. T is the temperature is set to 298.15 K.

The limiting potential (U_L) was adopted as a catalytic activity indicator to evaluate the CO₂RR performance of catalysts, which was obtained by $U_L = -\Delta G_{\text{max}}/e$ where ΔG_{max} presents the maximum ΔG of the elementary step corresponding to the potential determining step (PDS) in the reaction pathway.

RESULTS AND DISCUSSION

Synthesis and morphology characterizations

The synthesis process was illustrated in Figure 1A. MF was impregnated with an equal volume of nickel nitrate solution. The materials were freeze-dried and subsequently carbonized in a tube furnace at temperatures of 800, 900, and 1,000 °C with an atmosphere of argon. The carbonation products were collected and designated MF-Ni-800, MF-Ni-900, and MF-Ni-1000, respectively. Additionally, pure MF was

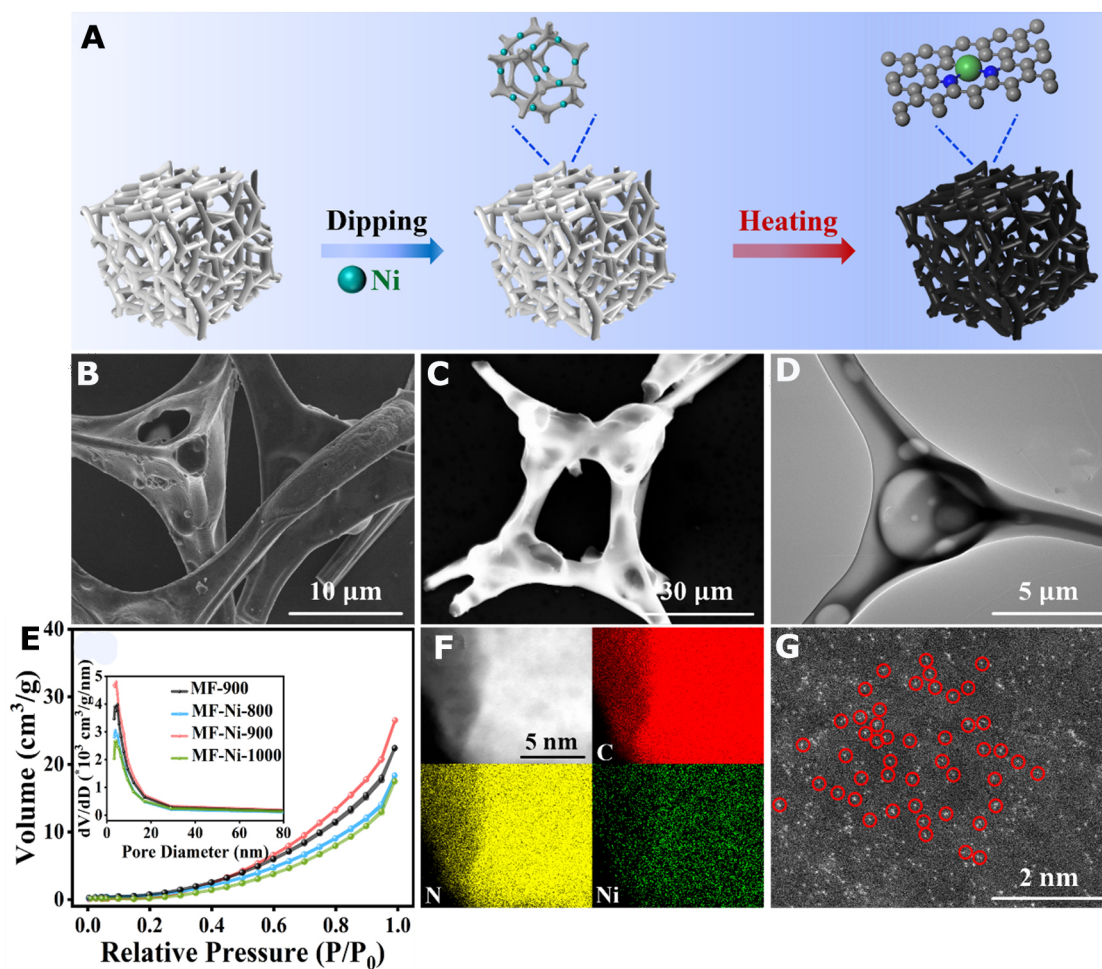


Figure 1. (A) Schematic diagram of catalyst synthesis; (B-D) SEM images (B-C), HR-TEM image (D) of MF-Ni-900; (E) N_2 adsorption and desorption curves and pore size distributions; (F) EDS images of MF-Ni-900; (G) AC-TEM image of MF-Ni-900. SEM: Scanning electron microscope; HR-TEM: high-resolution transmission electron microscope; MF: melamine foam; EDS: energy dispersive spectroscopy; AC-TEM: spherical aberration corrected transmission electron microscope.

obtained at 900 °C using the same synthesis method and was named MF-900. The porous network structure of MF allowed for a homogeneous dispersion of Ni atoms. Subsequent carbonization at different temperatures formed a Ni SAC with multiple active sites. It was a lightweight black foam that shrank in equal proportions [Supplementary Figure 1 and Supplementary Table 1].

Scanning electron microscopy (SEM) showed that MF-Ni-900 had a skeletal morphology of cross-linked structures [Figure 1B and C]. This suggested that MF could be used as a suitable support material to effectively confine nickel atoms within its porous structure, thus providing more active sites for CO_2RR . In Figure 1D and Supplementary Figure 2, it could be seen that a large number of pore-like structures suspected to be mesopores appeared at the cross-linked skeleton structure, which was in agreement with the results of later Brunauer-Emmett-Teller (BET) tests. Furthermore, the enhanced degree of skeleton shrinkage of MF-Ni-900 led to a denser material structure and a thinner conductive skeleton in comparison to that of MF-900 [Supplementary Figure 2]. Consequently, this resulted in a reduction in the path length for electron transport, thereby lowering the resistance and thus favoring electron transport.

The pore structure of the samples was determined by N₂ adsorption [Figure 1E]. The specific surface areas of MF-900, MF-Ni-800, MF-Ni-900, and MF-Ni-1000 were 17.2, 13.3, 20.7, and 12.2 m²/g, respectively. It could be observed that the specific surface area increased following the loading of Ni single atoms, which might be attributed to the fact that the anchoring of single atoms was typically dependent on defects in the carbon carrier (e.g., vacancies, edge sites or heteroatom doping sites). The majority of these strategies necessitated high-temperature calcination to facilitate the anchoring of atomic positions. The process of monoatomic anchoring during high-temperature treatment resulted in the formation of mesopores, thereby increasing the specific surface area. Furthermore, it was observed that the specific surface area exhibited variation when the Ni SAC was subjected to different carbonization temperatures. The increase in specific surface area as the carbonization temperature rises from 800 to 900 °C might be attributed to the complete decomposition of impurities blocking the ultra-microporous at 900 °C. As the carbonation temperature was increased to 1,000 °C, the specific surface area of the material was observed to decrease. This was attributed to the fact that the mechanical properties of MF were weakened by the elevated carbonization temperature, resulting in a collapse of the pore structure. The pore distribution, as calculated by the Barret-Joyner-Halenda (BJH) method, indicated that the pore size of the catalysts was predominantly distributed within the mesoporous range [Figure 1E]. The mesopores (2-50 nm) possessed a pore size that was conducive to the physical adsorption of CO₂ molecules. This process engendered a localized high concentration of gas-phase enrichment in the pore channels by means of capillary action. This was highly conducive to the transport, activation, and reduction of CO₂, which enhanced an increase in the concentration of CO₂ in the surrounding area.

Furthermore, energy dispersive spectroscopy (EDS) revealed the presence of Ni within MF-Ni-900 [Figure 1F]. The uniform dispersion of Ni atoms in MF-Ni-900 could be unambiguously demonstrated by means of spherical aberration corrected transmission electron microscopy (AC-TEM) [Figure 1G].

The crystal structure of the catalyst was characterized by XRD, as illustrated in Figure 2A. The XRD image showed peaks similar to those of amorphous carbon, with no visible metallic nickel particles or nickel compound peaks observed. This indicated a low nickel content on the carbon carrier, suggesting that the nickel was loaded on MF in monoatomic form. The broad peak observed at $2\theta = 25^\circ$ could be attributed to the (002) crystal plane of graphitic carbon. In contrast, the characteristic peak of the graphitic carbon (002) crystalline facet of MF-Ni-1000 was shifted to $2\theta = 25^\circ$, indicating the formation of a more ordered carbon structure at 1,000 °C. Furthermore, the XRD plot of MF-Ni-1000 exhibited an additional diffraction peak at 44° , which correlated with the (100) crystal plane of graphitic carbon. This indicated that the graphitization of the material might be intensified at elevated carbonization temperatures, resulting in the formation of ordered structures.

Subsequently, the material was subjected to Raman spectroscopy analysis [Figure 2B]. Two broad peaks were observed at 1,350 cm⁻¹ (D band) and 1,580 cm⁻¹ (G band) for the catalysts, which corresponded to amorphous carbon (D band) and sp² hybridization of graphitic carbon (G band), respectively. The graphitization coefficient (I_D/I_G) of the catalysts was above one, suggesting the presence of a highly defective local structure. As the carbonization temperature increased from 800 to 1,000 °C, the graphitization coefficient decreased from 1.17 to 1.04, indicating that the degree of graphitization increased at high carbonization temperatures. In contrast, the graphitization coefficient increased from 1.06 to 1.09 after loading monatomic nickel at the same carbonization temperature. This indicated a modification in the degree of graphitization and structure of MF-Ni-900 upon the addition of monatomic nickel, resulting in an increase in the number of defects present and thus providing a greater number of active sites.

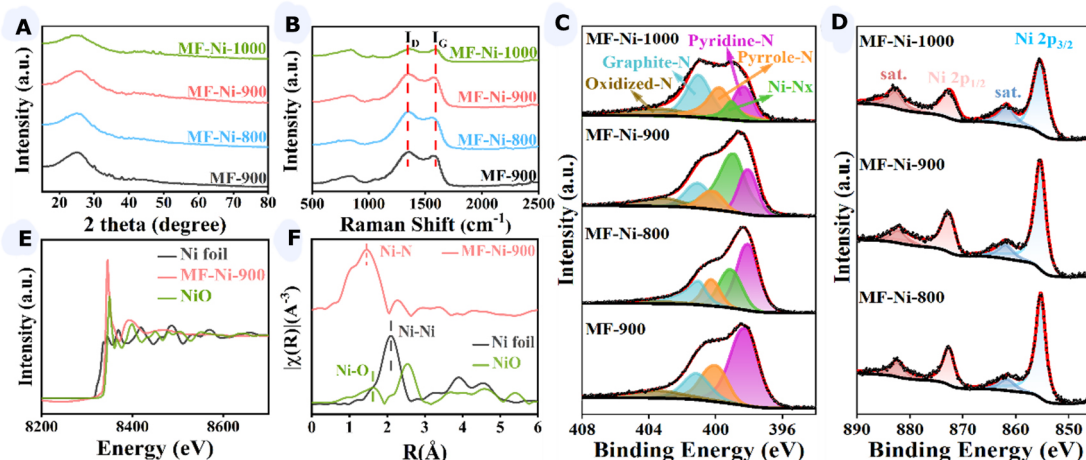


Figure 2. (A–C) XRD image (A), Raman image (B), N 1s spectrum of XPS image (C) of MF-900, MF-Ni-800, MF-Ni-900, and MF-Ni-1000; (D) Ni 2p spectrum of XPS image of MF-Ni-800, MF-Ni-900, and MF-Ni-1000; (E) Ni K-edge XANES spectra; (F) Fourier transform EXAFS spectra for MF-Ni-900, Ni foil, and NiO. XRD: X-ray diffraction; XPS: X-ray photoelectron spectroscopy; MF: melamine foam; XANES: X-ray absorption near edge structure; EXAFS: extended X-ray absorption fine structure.

The surface valence states between Ni single atoms and doped N were investigated by XPS. [Supplementary Figure 3](#) illustrated the complete XPS spectrum of the catalysts, which revealed the presence of sodium and oxygen in addition to the characteristic elements carbon, nitrogen, and nickel [[Supplementary Table 2](#)]. The presence of O might be attributed to the incorporation of formaldehyde during the synthesis of melamine formaldehyde resin or partial oxygen adsorption on the surface of the sample. The presence of Na was attributable to the addition of sodium hydroxide to adjust the pH of the solution during the synthesis of melamine-formaldehyde resin.

In the C 1s spectrum of XPS [[Supplementary Figure 4](#)], a peak with a binding energy of 284.8 eV was observed, which was typically associated with C–C bonds. Additionally, two peaks were present at 286.2 and 289.8 eV, which were attributed to C–O–C and O–C=O bonds, respectively^[31]. To ascertain whether there was an interaction between nitrogen and nickel atoms in the catalyst, we investigated the N 1s spectrum of XPS [[Figure 2C](#)] and compared it with the spectrum of MF-900. By fitting the N 1s spectra, four characteristic peaks were identified at 398.1, 400, 401.1, and 403.2 eV, which correspond to pyridine-N, pyrrole-N, graphite-N, and oxidized-N, respectively. The introduction of nickel atoms gave rise to the emergence of a novel component at 399.1 eV, accompanied by a reduction in the intensity of the pyridine-N spectral line^[32]. This indicated a transition from the pyridine-N to the Ni–N_x state. In the N 1s spectra [[Supplementary Table 3](#)], the Ni–N_x content of MF-Ni-900 accounted for 9.47 at.% of the total, which was significantly higher than that in MF-Ni-800 (5.85 at.%) and MF-Ni-1000 (3.95 at.%). At lower temperatures (MF-Ni-800), there was a reduction in the amount of carbon carrier defects and consequently, a reduction in the amount of nickel atom anchoring. At higher temperatures (MF-Ni-1000), the pore structure within the carbon skeleton collapses, leading to reduced M–N_x binding. This finding aligned with the results reported in the BET study. Consequently, it could be hypothesized that the superior CO₂RR performance of MF-Ni-900 was attributable to its elevated Ni–N_x content.

[Figure 2D](#) illustrated the binding energies of Ni 2p_{3/2} and Ni 2p_{1/2}, which were observed to be centered at 855.4 and 872.7 eV, respectively. The positions of the spectral lines of Ni 2p were similar to those of N-doped monatomic nickel catalysts. It could be speculated that Ni in the catalyst was individual Ni atoms rather than nanoparticles^[33]. Furthermore, the Ni 2p_{3/2} peak in the catalyst exhibited a positive shift of

approximately 0.2 eV in comparison to the standard Ni $2p_{3/2}$ peak (855.6 eV), which suggested that Ni possessed an electron-donor nature. Meanwhile, the N 1s peak in the catalyst exhibited disparate degrees of negative shifts in comparison with the standard peak, indicating that the N site was an electron acceptor. The findings suggested that Ni atoms with a high electron density could provide a greater number of electrons to the electron-deficient N, thereby balancing the electronic configuration. This was conducive to the transfer of electrons and reaction kinetics in the electrocatalytic process. In order to further investigate the valence of the Ni atomic structure, X-ray absorption near edge structure (XANES) analysis was performed. The XANES results at the Ni K-edge were illustrated in [Figure 2E](#), with Ni foil and NiO used as references. The absorption edge of Ni in MF-Ni-900 was found to be very close to that of NiO, indicating that the average valence state of Ni was +2. This finding was in accordance with the results obtained by means of XPS analysis. The local coordination environment of the atomic structure in question could be revealed from the Fourier transform extended X-ray absorption fine structure (FT-EXAFS) spectra [[Figure 2F](#)]. The major peak of MF-Ni-900 was located at 1.45 Å, which proved the presence of Ni-N_x coordination in MF-Ni-900, in agreement with the results of the XPS split-peak fitting. It was noteworthy that the signal of Ni-Ni (2.13 Å) was not detected, indicating that Ni was atomically dispersed in MF-Ni-900.

The post-reaction SEM, XRD and XPS measurements were conducted to ascertain whether there were alterations on catalysts before and after the reaction. As illustrated in [Supplementary Figure 5A](#), the SEM image revealed that the melamine skeleton exhibited no signs of cracking or pitting following the reaction. This finding suggested that it was well-stabilized, making it suitable for use as a carbon carrier for the loading of single atoms. Furthermore, the presence of flakes or lumps on the surface of the skeleton might be attributable to carbonate precipitation without thorough washing. As demonstrated in [Supplementary Figure 5B](#), the post-reaction XRD plot displayed peaks and shapes consistent with those of amorphous carbon as observed in the pre-reaction XRD plot. Furthermore, no peaks indicative of Ni particles were evident. This finding suggested that the reacted Ni active sites did not agglomerate and persist as individual atoms, thereby further substantiating the catalyst's stability. In order to ascertain whether a change in the valence state of the Ni atoms had occurred, post-reaction XPS tests were performed. The N 1s plot following peak splitting [[Supplementary Figure 5C](#)] demonstrated that the quantity of pyridine N decreased whilst the quantity of pyrrole N increased, and the quantity of other types of N remained almost unchanged. This phenomenon might be attributed to the hydrogenation of pyridine N to form a pyrrole N structure by the addition of H in a reducing reaction environment. Furthermore, the coordination structure of the active site remained intact during the reaction, indicating that the Ni-N bond was not broken and its catalytic property was retained. The Ni 2p spectra were fitted as shown in [Supplementary Figure 5D](#). The half-peak widths of Ni $2p_{3/2}$ and Ni $2p_{1/2}$ were consistent with the pre-reaction values and did not show peaks of Ni particles. This finding excluded the possibility of Ni reduction or oxidation and provided further evidence that Ni existed as a single atom.

Electrochemical test in H-cell

The activity of the catalysts for electrocatalytic CO₂RR was investigated in an H-type electrolytic cell, with the electrodes separated by the Nafion 117 membrane. [Figure 3A](#) demonstrated that the catalysts exhibited considerable cathodic current densities in CO₂-saturated electrolytes at potentials ranging from 0.54 to -1.16 V vs. RHE. These values were markedly higher than those observed in Ar-saturated electrolytes. This suggested that the catalyst exhibited a preference for the activation of CO₂ molecules over that of protons, thereby indicating an excellent capability for CO₂RR. The j_{CO} values were then normalized using electrochemically active surface area (ECSA) in order to eliminate the effect of non-intrinsic factors. As demonstrated in [Supplementary Figure 6](#), the normalized curve exhibited a congruent trend with the normal linear scanning voltammetry (LSV) curve [[Figure 3A](#)]. This indicated that MF-Ni-900 also had

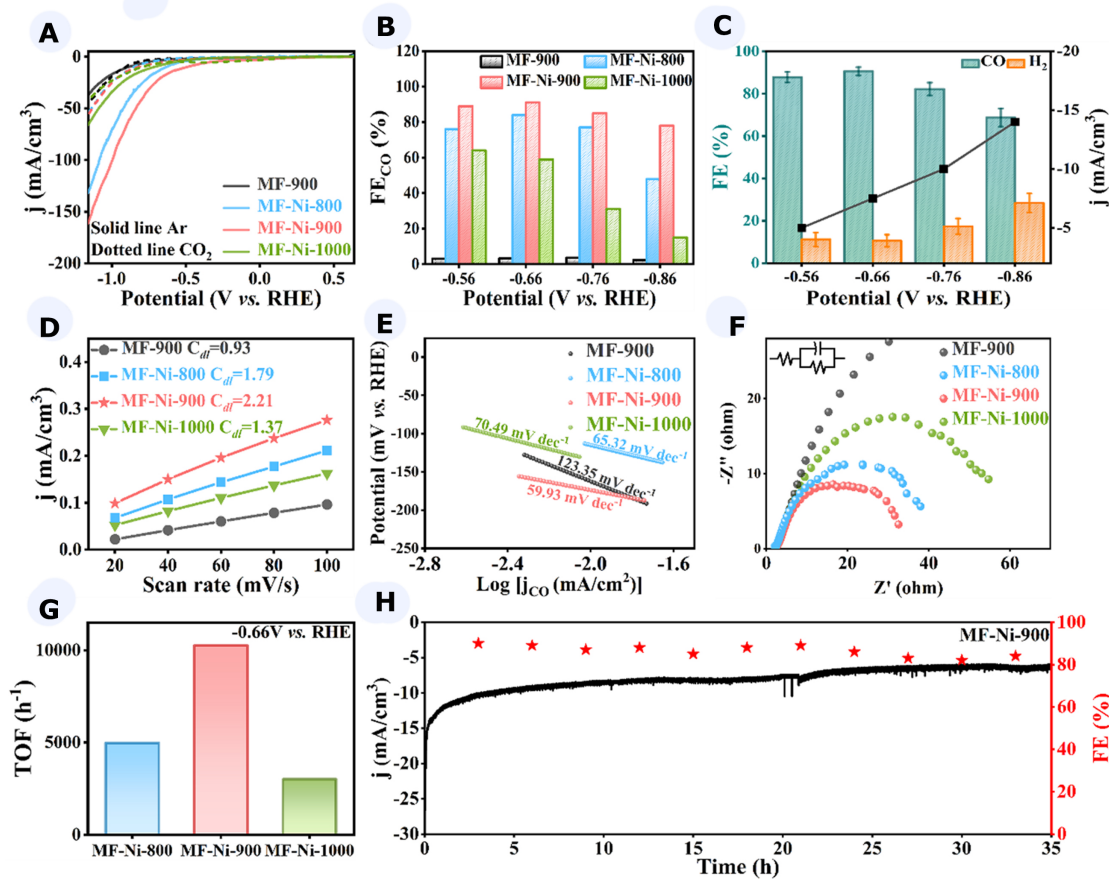


Figure 3. (A) Linear sweep voltammetry (LSV) image of catalysts in Ar-saturated or CO₂-saturated 0.5 M KHCO₃ electrolytes; (B) FE_{CO} image of catalysts at -0.56 to -0.86 V vs. RHE potentials; (C) CO Faradaic efficiency error bars and current density image of MF-Ni-900; (D-G) ECSA linear image (D), Tafel image (E), EIS image (F), TOF image (G) of MF-900, MF-Ni-800, MF-Ni-900, and MF-Ni-1000; (H) 35 h long-term stability of MF-Ni-900. FE_{CO}: Faradaic efficiency of CO; RHE: reversible hydrogen electrode; MF: melamine foam; ECSA: electrochemically active surface area; EIS: electrochemical impedance spectroscopy; TOF: transition frequency.

higher catalytic performance at the same unit active site.

To provide further evidence of the CO₂RR performance of MF-Ni-900, the reduction products and corresponding FE of the catalyst at varying potentials were subjected to quantitative analysis via online gas chromatography (GC), as illustrated in Figure 3B. At -0.66 V vs. RHE, MF-Ni-900 exhibited a current of -7.5 mA/cm² and FE_{CO} of 91%, which was superior to that of MF-Ni-800 (84.6%) and MF-Ni-1000 (59.1%). It was worthy of note that the FE_{CO} of MF-Ni-900 was markedly higher than that of MF-900 catalyst. These findings indicated that the incorporation of a Ni component in MF-Ni-900 was the primary factor responsible for the enhancement of CO₂RR activity. In order to evaluate the performance advantages of MF-Ni-900 catalyst, a systematic comparison of the activity data of typical CO₂RR catalysts reported in recent years was conducted [Supplementary Table 4]. The comparison yielded that MF-Ni-900 catalyst had superior CO selectivity and current density. This finding lent further credence to the hypothesis that high active site density could enhance catalytic efficiency. Figure 3C illustrated the Faradaic efficiency error bars and current density plots of CO and H₂ for MF-Ni-900 within the range of -0.56 to -0.86 V vs. RHE. It could be observed that there was minimal variation in the FE, accompanied by a substantial current, which indicated that the catalyst was well-stabilized and exhibited excellent performance in CO₂RR. After that, we tested the FE of melamine powder loaded with Ni single atoms at the same potential was tested

[Supplementary Figure 7]. It was evident that the FE of CO was significantly lower than that of MF-Ni-900. This finding suggested that the porous three-dimensional skeleton facilitated the formation of more Ni-N_x bonds during the high-temperature calcination process, which in turn enhanced the catalytic activity of CO₂ RR for the generation of CO. The electrochemical performance further validated the results of the previous BET and XPS tests.

To ascertain the reasons for the excellent CO₂RR performance, a test was conducted into the electrochemical active surface area (ECSA) of the catalysts. This was accomplished by assessing the ECSA through the quantification of the double-layer capacitance (C_{dl}) at varying scan rates on the cyclic voltammetry curves [Supplementary Figure 8]. As illustrated in Figure 3D, MF-Ni-900 exhibited the highest C_{dl} of 2.21 mF·cm⁻³. This finding indicated that the Ni-N_x content in MF-Ni-900 was proportional to C_{dl} , thereby substantiating the validity of our hypothesis derived from XPS analysis. Furthermore, for electrochemical reactions, an enlarged active surface area of the electrode signified a magnified effective area on the electrode where the reaction could occur, resulting in an augmented reaction rate and current density, which was more conducive to the CO₂RR.

The Tafel curves of the catalysts were plotted [Figure 3E]. The Tafel slope (b) of MF-Ni-900 was 59.93 mV·dec⁻¹, which was markedly smaller than that of MF-Ni-800 (65.32 mV·dec⁻¹) and MF-Ni-1000 (70.49 mV·dec⁻¹), and much smaller than that of MF-900 (123.35 mV·dec⁻¹). A smaller value of slope b indicated that the reaction was more sensitive to overpotential (i.e., small overpotential could drive a large current) and the kinetic rate was faster. This suggested that MF-Ni-900 catalyst exhibited a higher kinetic rate and greater kinetic activity in the generation of CO. The charge transfer resistance (R_{ct}) of the catalyst was determined using electrochemical impedance spectroscopy (EIS) and an equivalent circuit was fitted. It had been demonstrated that the R_{ct} was proportional to the diameter of the semicircular Nyquist diagram. As demonstrated in Figure 3F, the semicircle diameter of MF-Ni-900 was more diminutive than that of the other catalysts, thus indicating that it possessed the lowest R_{ct} . This also indicated that MF-Ni-900 catalyst displayed superior conductivity and charge transfer kinetics in comparison to other catalysts, which were essential for the formation of intermediates in the CO₂RR.

In order to ascertain the true catalytic capacity of the catalyst, an inductively coupled plasma test (ICP) was performed to calculate the TOF of the catalyst. As illustrated in Figure 3G, the maximum turnover frequency of MF-Ni-900 at -0.66 V vs. RHE reached 10,266 h⁻¹, a value that was considerably higher than the TOF values of MF-Ni-800 (4,976 h⁻¹) and MF-Ni-1000 (3,007 h⁻¹). This finding suggested that MF-Ni-900 exhibited superior intrinsic activity and could convert reactants more rapidly under identical conditions. The cathodic energy efficiency (CEE) for CO generation was 74.7% at -0.66 V vs. RHE, which was comparable to the CEE values reported for the most recently developed Ni-based monoatomic catalysts. The durability of the catalyst was a further crucial factor in the assessment of electrocatalytic performance. As illustrated in Figure 3H, the current density remained largely unaltered after 35 h, and the FE_{CO} exhibited only a modest decline and sustained a high value (FE_{CO} > 80%). The electrochemical performance of MF-Ni-900 was tested across six cycles [Supplementary Figure 9], revealing that the catalyst maintained a stable current density and FE after six cycles. These findings suggested that MF-Ni-900 exhibited both high durability and reversibility.

The ATR-SEIRAS

In order to detect the reaction mechanism of CO₂RR, *in situ* attenuated total reflectance surface-enhanced infrared absorption spectroscopy (ATR-SEIRAS) was conducted to monitor the catalytic reaction route and intermediates. We designed a three-electrode reaction device similar to an H-type electrolytic cell and tested

it in CO₂-saturated 0.5 M KHCO₃ aqueous solution. The experimental evidence indicated that *CO and *COOH were produced in the reaction pathway that produced CO. Furthermore, the concentrations of the surface intermediates *COOH and *CO were observed to vary with increasing negative potentials [Figure 4A-D].

In situ IR revealed the presence of an HCO₃⁻ stretching peak at approximately 1,210 cm⁻¹, which was attributed to the adsorption of electrolyte on the catalyst surface. It was observed that the depletion of HCO₃⁻ increased in accordance with the rising test potential, which suggested that HCO₃⁻ was converted to CO₃²⁻ to generate carbonate.

The positive peak observed at approximately 1,400 cm⁻¹ was attributed to the stretching of the C-O bond in the bidentate functional group, *COOH. The intensity of the *COOH signal demonstrated a gradual increase with increasing potential from -0.16 to -1.06 V vs. RHE. It was noteworthy that the *COOH peak intensity of MF-Ni-900 was more pronounced than that observed on the other catalysts and appeared earlier in the potential. This finding suggested that the Ni-N_x active site exerted a favorable effect on the adsorption and activation of H₂O and CO₂ molecules, thereby facilitating the generation and adsorption of *COOH intermediates. Moreover, the positive peak observed at 1,630 cm⁻¹ was indicative of the bending of the H-O-H bond in water. At extremely high potentials, the intensity of the water peak increased with rising potential, while the intensity of the *CO peak decreased with increasing potential. This suggested that the HER was the dominant process at these extremely high potentials.

The peaks at 1,930 and 2,118 cm⁻¹ in the *in situ* IR spectrum were indicative of the bridging CO adsorption (CO_B) species and the telescoping vibrations of linear CO (CO_L), respectively. MF-Ni-900 exhibited the earliest and most pronounced appearance of CO_B peaks, suggesting that it displayed greater selectivity for *CO generation. Furthermore, the CO_B peak exhibited a shift towards lower wave numbers when the potential became large. This was a consequence of the Stark effect, which intensified the interaction between *CO and the catalyst^[34,35]. This also confirmed that the observed *CO was a surface-absorbed substance and not a dissolved molecule. The intensity of the CO_L peak displayed an initial increase, followed by a subsequent decrease, which could be attributed to CO_L converted to CO_B at high potentials. It could be observed that the *COOH peak was barely discernible when the CO_B peak was present at lower potentials. This indicated that the production of *COOH and subsequent protonation with H⁺ resulted in the formation of *CO. Therefore, the decisive step of the reaction was the protonation of CO₂ to form a *COOH intermediate.

To further substantiate the assertion that Ni-N_x was the active site, a linear fit was conducted on the peak area and Ni-N_x content of CO_B [Figure 4E]. It could be observed that there was a strong linear relationship between the peak area of CO_B and the Ni-N_x content at all the potentials that were tested. It could thus be concluded that Ni-N_x was the active center of the catalysts and that CO_B was the key intermediate in the CO₂RR.

The results of *in situ* IR indicated that the adsorption and activation of CO₂ and water molecules on Ni-N_x active sites promoted the formation of *COOH, which accelerated the conversion of CO₂ to CO. A mechanism for the CO₂RR was therefore proposed as follows: first, CO₂ was adsorbed on the catalyst, resulting in the initial electron transfer to form a *CO₂⁻ intermediate; subsequently, *CO₂⁻ protonated to form *COOH, with the H⁺ derived from H₂O. Finally, *COOH was dehydrated to form a *CO intermediate on the surface and then desorbed to form the target product [Figure 4F].

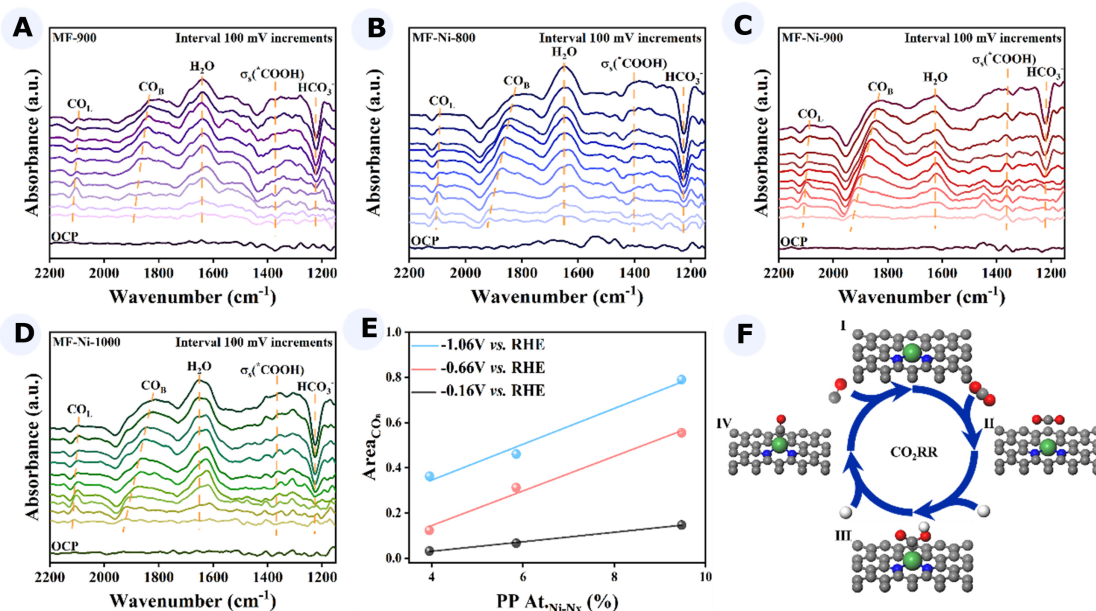


Figure 4. (A–D) At -0.16 to -1.06 V vs. RHE potentials, *in situ* IR images of MF-900 (A), MF-Ni-800 (B), MF-Ni-900 (C), and MF-Ni-1000 (D); (E) Linear relationship between CO_B peak area and Ni-N_x content; (F) Mechanism diagram of CO₂ to CO. RHE: Reversible hydrogen electrode; IR: infrared spectroscopy; MF: melamine foam; CO_B: CO adsorption.

Density functional theory calculations

In order to gain further insight into the electrocatalytic CO₂RR behavior of Ni-N_x, we adopted DFT calculations in this work. Previous studies had concluded that Ni-N₂, Ni-N₃, and Ni-N₄ were stable coordination structures of Ni at different N concentrations in synthetic processes^[36]. Therefore, the active sites on the Ni-N_x surface that we considered include gra, gra-N, Ni-N₂, Ni-N₃, and Ni-N₄ [Figure 5A]. Particularly, it could be found that Ni-N₂ had three possible initial configurations (Ni-N₂-1, Ni-N₂-2, and Ni-N₂-3), of which Ni-N₂-1 had the lowest energy with superior stability. Thus, Ni-N₂-1 was selected for subsequent Ni-N₂ related studies.

The calculated Gibbs free energy profile of CO₂RR to CO on the catalysts (gra, gra-N, Ni-N₂, Ni-N₃, and Ni-N₄) was shown in Figure 5B. The CO₂ adsorption strengths of Ni-N_x catalysts exhibited negligible differences, suggesting their comparable CO₂ activation capabilities. The O atoms of ^{*}CO₂ preferred to combine with H to form ^{*}COOH (^{*}CO₂ + H⁺ + e⁻ → ^{*}COOH), which was the PDS of CO₂RR to CO on these catalysts. Among them, Ni-N₂ overcame the least energy in PDS (*U_L* = -0.87 V). Therefore, the key active site of CO₂RR on Ni-N_x was Ni-N₂. The last hydrogenation step was an energy downhill elementary reaction (^{*}COOH + H⁺ + e⁻ → ^{*}CO + H₂O) with the release of H₂O. Finally, the ^{*}CO was desorbed from the catalyst surface to generate the CO as the final product.

The crystal orbital Hamilton populations (COHP) between ^{*}COOH (one of the intermediates in PDS) and the active sites were then calculated [Figure 5C and D] to reveal the activity origin of CO₂RR on these catalysts. It was evident that the bonding states of ^{*}COOH and active sites on catalysts occurred below the Fermi level. Therefore, the bonding states were filled with electrons, which led to a strong interaction between the active sites and ^{*}COOH. The performance of Ni-N_x was governed by the energy change of ^{*}CO₂ + H⁺ + e⁻ → ^{*}COOH. Due to the minimal variation in CO₂ adsorption strengths across Ni-N_x active sites, the catalytic performance predominantly depended on the interaction strength between ^{*}COOH intermediates and Ni-N_x sites. The enhanced interaction between ^{*}COOH and the active site corresponded

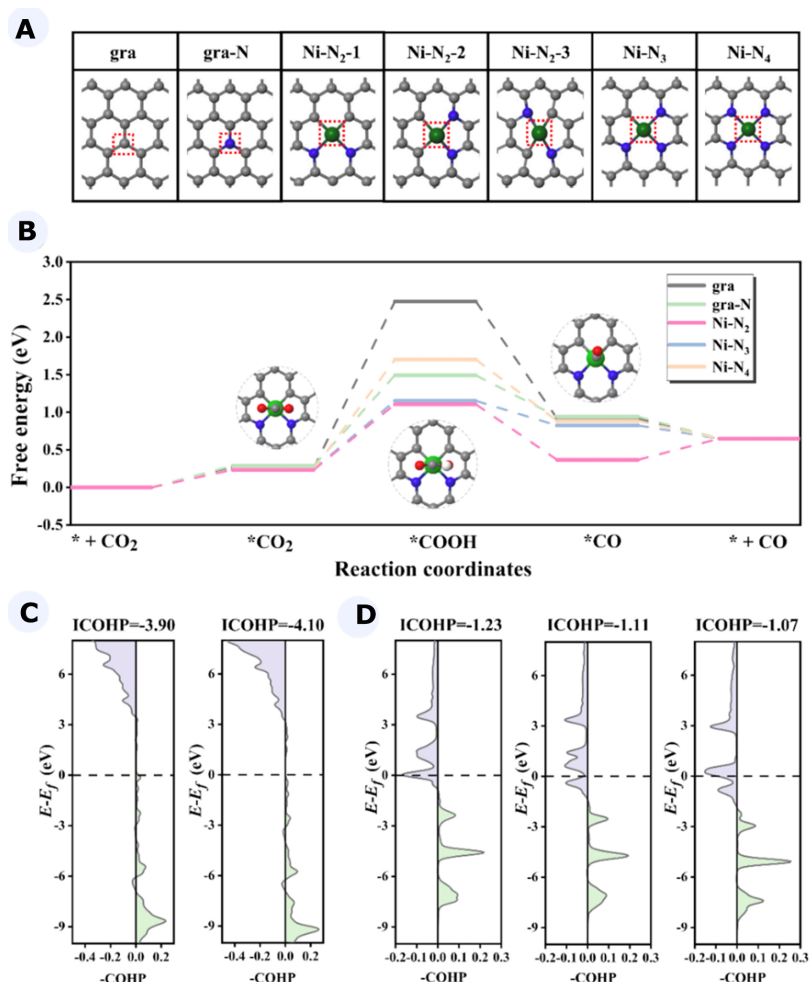


Figure 5. (A) The optimized structures of different active sites on the Ni-N_x surface; (B) The Gibbs free energy profile of CO₂RR to CO on gra, gra-N, Ni-N₂, Ni-N₃, and Ni-N₄. The COHP for COOH adsorbed on active site of (C) gra and gra-N, (D) Ni-N₂, Ni-N₃, and Ni-N₄. CO₂RR: Carbon dioxide reduction reaction; COHP: crystal orbital Hamilton populations.

to the more negative energy of *COOH, thereby reducing the PDS energy barrier and enhancing catalytic activity. Within the Ni-N_x system, active centers could be classified into metal sites (Ni-N₂, Ni-N₃, and Ni-N₄) and non-metal sites (gra and gra-N). Among non-metal sites, in Figure 5C, gra-N demonstrated a more negative integrated COHP (ICOHP) value (-4.10) with *COOH than gra (-3.90), indicating stronger bonding and enhanced stabilization of *COOH on gra-N. As shown in Figure 5D, the Ni-N₂, Ni-N₃, and Ni-N₄ yielded ICOHP values of -1.23, -1.11, and -1.07, respectively, with *COOH. Notably, Ni-N₂ displayed the most negative ICOHP value, reflecting the strongest bonding with *COOH. Meanwhile, the *COOH adsorption strength of Ni-N₂ was superior to that of gra-N [Figure 5B]. Therefore, the unique coordination environment of the Ni-N₂ site resulted in the greatest interaction strength with *COOH intermediate, corresponding to the lowest PDS energy change, the least negative U_L , and the most favorable catalytic performance.

In conclusion, the results of DFT calculations indicated that Ni-N₂ served as the active site that played a significant role in Ni-N_x.

CONCLUSIONS

In conclusion, the successful synthesis of Ni single-atom foam catalysts with multiple active sites was achieved by means of an impregnation-carbonation approach. The findings demonstrated that the highly cross-linked structure of MF provided a substantial amount of space for the escape of the product, which not only enhanced the dispersion of the active site but also facilitated electron transport. The content of Ni-N_x bonds formed was contingent upon the carbonation temperature, which in turn influenced the electrochemical functionality of the catalysts. It was observed that MF-Ni-900 exhibited excellent dispersion of metal atoms and displayed high selectivity for CO₂RR, with an FE_{CO} of 91% and a *j*_{CO} of 6.83 mA·cm⁻³. Performance remained essentially unchanged after 35 h of stability testing. Furthermore, *in situ* IR was conducted to investigate the intermediates of CO generation from CO₂RR and to elucidate the underlying reaction mechanism. Based on theoretical calculations, we found that among all active site candidates, the coordination of Ni-N₂ was more favorable to achieve a proper interaction between COOH and the active site with a minimum energy change in PDS of CO₂RR (*U*_L = -0.87 V), suggesting Ni-N₂ played a critical role in promising the CO₂RR performance of Ni-N_x. This study provides a comprehensive description of the active sites of the N-coordinated Ni SACs and demonstrates that the optimal catalytic performance is achieved when the Ni-N_x bond content is at its maximum, which provides some theoretical guidance for the construction of SACs in the future.

DECLARATIONS

Acknowledgments

We would like to acknowledge the technical support from Analysis and Testing Center of Northeast Forestry University.

Authors' contributions

Made substantial contributions to the conception and design of the study, performed data analysis and interpretation, and wrote original draft: Wei, A.; Xu, Y.

Conducted the investigation of the study and performed data acquisition: Wang, J.; Shi, L.

Revised the manuscript and provided administrative, technical, and material support: Liu, S.; Wu, Y.; Wang, W.

Availability of data and materials

The detailed experimental methods and data are available from [Supplementary Materials](#).

Financial support and sponsorship

This work was financially supported by the National Natural Science Foundation of China (22208048, 22172044, and 22478067), the National Key R&D Program of Heilongjiang Province, China (2022ZX02C23), the Natural Science Foundation of Heilongjiang Province (YQ2022B005), the Young Elite Scientists Sponsorship Program by CAST (YESS20210262), the Fundamental Research Funds for the Central Universities (2572023CT10).

Conflicts of interest

All authors declared that there are no conflicts of interest.

Ethical approval and consent to participate

Not applicable.

Consent for publication

Not applicable.

Copyright

© The Author(s) 2025.

REFERENCES

1. Chen, P. C.; Chen, C.; Yang, Y.; et al. Chemical and structural evolution of AgCu catalysts in electrochemical CO₂ reduction. *J. Am. Chem. Soc.* **2023**, *145*, 10116–25. DOI PubMed
2. Guo, H.; Si, D. H.; Zhu, H. J.; Chen, Z. A.; Cao, R.; Huang, Y. B. Boosting CO₂ electroreduction over a covalent organic framework in the presence of oxygen. *Angew. Chem. Int. Ed. Engl.* **2024**, *63*, e202319472. DOI PubMed
3. Yang, X.; Yang, J.; Zhao, T.; et al. Kinetic insights into the effect of promoters on Co/Al₂O₃ for Fischer-Tropsch synthesis. *Chem. Eng. J.* **2022**, *445*, 136655. DOI
4. Wan, X.; Li, Y.; Chen, Y.; et al. A nonmetallic plasmonic catalyst for photothermal CO₂ flow conversion with high activity, selectivity and durability. *Nat. Commun.* **2024**, *15*, 1273. DOI PubMed PMC
5. Li, S.; Kan, Z.; Wang, H.; et al. Single-atom photo-catalysts: synthesis, characterization, and applications. *Nano. Mater. Sci.* **2024**, *6*, 284–304. DOI
6. Wang, J.; Huang, Y. C.; Wang, Y.; et al. Atomically dispersed metal-nitrogen-carbon catalysts with d-orbital electronic configuration-dependent selectivity for electrochemical CO₂-to-CO reduction. *ACS. Catal.* **2023**, *13*, 2374–85. DOI
7. Zeng, Y.; Zhao, J.; Wang, S.; et al. Unraveling the electronic structure and dynamics of the atomically dispersed iron sites in electrochemical CO₂ reduction. *J. Am. Chem. Soc.* **2023**, *145*, 15600–10. DOI PubMed
8. Akula, S.; Mooste, M.; Kozlova, J.; et al. Transition metal (Fe, Co, Mn, Cu) containing nitrogen-doped porous carbon as efficient oxygen reduction electrocatalysts for anion exchange membrane fuel cells. *Chem. Eng. J.* **2023**, *458*, 141468. DOI
9. Murphy, E.; Liu, Y.; Matanovic, I.; et al. Elucidating electrochemical nitrate and nitrite reduction over atomically-dispersed transition metal sites. *Nat. Commun.* **2023**, *14*, 4554. DOI PubMed PMC
10. Zhao, Z.; Shi, X.; Shen, Z.; et al. Single-atom Fe nanozymes coupling with atomic clusters as superior oxidase mimics for ratiometric fluorescence detection. *Chem. Eng. J.* **2023**, *469*, 143923. DOI
11. Liu, H.; Zhu, P.; Yang, D.; et al. Pd-Mn/NC dual single-atomic sites with hollow mesopores for the highly efficient semihydrogenation of phenylacetylene. *J. Am. Chem. Soc.* **2024**, *146*, 2132–40. DOI PubMed
12. Zhang, D.; Wang, Z.; Liu, F.; et al. Unraveling the pH-dependent oxygen reduction performance on single-atom catalysts: from single- to dual-Sabatier optima. *J. Am. Chem. Soc.* **2024**, *146*, 3210–9. DOI PubMed PMC
13. Liu, Y.; Li, C.; Loubidi, M.; et al. Increasing exposure of atomically dispersed Ni sites via constructing hierarchically porous supports for enhanced electrochemical CO₂ reduction. *Chem. Eng. J.* **2021**, *426*, 131414. DOI
14. Pan, F.; Zhang, H.; Liu, K.; et al. Unveiling active sites of CO₂ reduction on nitrogen-coordinated and atomically dispersed iron and cobalt catalysts. *ACS. Catal.* **2018**, *8*, 3116–22. DOI
15. Wang, X.; Li, X.; Ding, S.; et al. Constructing ample active sites in nitrogen-doped carbon materials for efficient electrocatalytic carbon dioxide reduction. *Nano. Energy.* **2021**, *90*, 106541. DOI
16. Bai, J.; Sun, Z.; Zhang, H.; et al. Modulating the local coordination environment of M-N_x single-atom site for enhanced electrocatalytic oxygen reduction. *Adv. Funct. Mater.* **2025**, *35*, 2417013. DOI
17. Huang, Z. Y.; Guo, X. S.; Tang, Y.; Ye, J. S.; Liu, H. Y.; Xiao, X. Y. Metalloporphyrin doped macroporous ZIF-8 metal-organic framework derived M-N_x carbon material for oxygen reduction reactions. *J. Alloy. Compd.* **2023**, *947*, 169441. DOI
18. Miao, Z.; Li, S.; Priest, C.; Wang, T.; Wu, G.; Li, Q. Effective approaches for designing stable M-N_x/C oxygen-reduction catalysts for proton-exchange-membrane fuel cells. *Adv. Mater.* **2022**, *34*, e2200595. DOI PubMed
19. Xi, D.; Li, J.; Low, J.; et al. Limiting the uncoordinated N species in M-N_x single-atom catalysts toward electrocatalytic CO₂ reduction in broad voltage range. *Adv. Mater.* **2022**, *34*, e2104090. DOI PubMed
20. Devi, H. R.; Bisen, O. Y.; Chen, Z.; Nanda, K. K. Spatially dispersed one-dimensional carbon architecture on oxide framework for oxygen electrochemistry. *Chem. Eng. J.* **2022**, *433*, 133649. DOI
21. Hu, H.; Gao, G. H.; Xiao, B. B.; Zhang, P.; Mi, J. L. The oxygen reduction reaction activity and selectivity of porous-carbon supported transition metals (M-C: M = Mn, Fe, Co, Ni, Cu) electrocatalysts. *Diam. Relat. Mater.* **2023**, *134*, 109776. DOI
22. Jiang, T.; Jiang, H.; Wang, W.; Mu, H.; Zhang, Y.; Li, B. Atomically dispersed high-active site density copper electrocatalyst for the reduction of oxygen. *Materials* **2024**, *17*, 5030. DOI PubMed PMC
23. Kresse, G.; Furthmüller, J. Efficient iterative schemes for *ab initio* total-energy calculations using a plane-wave basis set. *Phys. Rev. B. Condens. Matter.* **1996**, *54*, 11169–86. DOI PubMed
24. Kresse, G.; Furthmüller, J. Efficiency of *ab-initio* total energy calculations for metals and semiconductors using a plane-wave basis set. *Comput. Mater. Sci.* **1996**, *6*, 15–50. DOI
25. Blöchl, P. E. Projector augmented-wave method. *Phys. Rev. B. Condens. Matter.* **1994**, *50*, 17953–79. DOI PubMed
26. Kresse, G.; Joubert, D. From ultrasoft pseudopotentials to the projector augmented-wave method. *Phys. Rev. B.* **1999**, *59*, 1758–75.

DOI

27. Perdew, J. P.; Burke, K.; Ernzerhof, M. Generalized gradient approximation made simple. *Phys. Rev. Lett.* **1996**, *77*, 3865-8. DOI PubMed
28. Grimme, S.; Antony, J.; Ehrlich, S.; Krieg, H. A consistent and accurate *ab initio* parametrization of density functional dispersion correction (DFT-D) for the 94 elements H-Pu. *J. Chem. Phys.* **2010**, *132*, 154104. DOI PubMed
29. Grimme, S.; Ehrlich, S.; Goerigk, L. Effect of the damping function in dispersion corrected density functional theory. *J. Comput. Chem.* **2011**, *32*, 1456-65. DOI PubMed
30. Nørskov, J. K.; Rossmeisl, J.; Logadottir, A.; et al. Origin of the overpotential for oxygen reduction at a fuel-cell cathode. *J. Phys. Chem. B.* **2004**, *108*, 17886-92. DOI PubMed
31. Hou, Y.; Qiu, M.; Kim, M. G.; et al. Atomically dispersed nickel-nitrogen-sulfur species anchored on porous carbon nanosheets for efficient water oxidation. *Nat. Commun.* **2019**, *10*, 1392. DOI PubMed PMC
32. Yan, C.; Li, H.; Ye, Y.; et al. Coordinatively unsaturated nickel-nitrogen sites towards selective and high-rate CO₂ electroreduction. *Energy. Environ. Sci.* **2018**, *11*, 1204-10. DOI
33. Feng, Y.; Long, S.; Chen, B.; et al. Inducing electron dissipation of pyridinic N enabled by single Ni-N₄ sites for the reduction of aldehydes/ketones with ethanol. *ACS. Catal.* **2021**, *11*, 6398-405. DOI
34. Delmo, E. P.; Wang, Y.; Song, Y.; et al. *In Situ* infrared spectroscopic evidence of enhanced electrochemical CO₂ reduction and C-C coupling on oxide-derived copper. *J. Am. Chem. Soc.* **2024**, *146*, 1935-45. DOI PubMed
35. Deng, B.; Huang, M.; Li, K.; et al. The crystal plane is not the key factor for CO₂-to-methane electrosynthesis on reconstructed Cu₂O microparticles. *Angew. Chem. Int. Ed. Engl.* **2022**, *61*, e202114080. DOI PubMed
36. Wang, H.; Li, Y.; Wang, M.; et al. Precursor-mediated *in situ* growth of hierarchical N-doped graphene nanofibers confining nickel single atoms for CO₂ electroreduction. *Proc. Natl. Acad. Sci. U. S. A.* **2023**, *120*, e2219043120. DOI PubMed PMC



Anqi Wei

Anqi Wei is currently pursuing a Master's degree in Chemistry at Northeast Forestry University, where she also earned her B.S. degree in 2023. Her research focuses on the electrocatalytic reduction of carbon dioxide and its underlying mechanisms.



Yang Xu

Yang Xu is a Ph.D. candidate in Chemistry at Northeast Forestry University. She received her B.S. degree in Chemistry from the same institution in 2024. Her research centers on density functional theory (DFT) simulations of the electrocatalytic CO₂ reduction reaction.



Jiangfang Wang

Jiangfang Wang is pursuing a Master's degree in Chemistry at Northeast Forestry University. She obtained her B.S. degree from the same university in 2022. Her research interests include electrocatalytic carbon dioxide reduction and mechanistic studies.



Lei Shi

Lei Shi is a Ph.D. student in Biology at Northeast Forestry University. He earned his M.S. degree from the same university in 2020. His research focuses on developing enzyme-mimicking catalysts and investigating the electrocatalytic conversion of biomass-derived small molecules.



Chong Wang

Chong Wang received his Ph.D. in Physical Chemistry from Jilin University and is currently affiliated with Northeast Forestry University. His research interests include catalyst design, reaction mechanism exploration, and first-principles calculations in electrocatalysis and computational chemistry.

**Yingjie Wu**

Yingjie Wu is a professor and doctoral supervisor at Harbin Institute of Technology. She has been selected as a Longjiang Young Scholar, a recipient of the Heilongjiang Province Outstanding Young Project, and a Harbin Institute of Technology Young Elite Talent. Her research focuses on the design, synthesis, and catalytic regulation of supramolecular assemblies. She has authored 45 academic papers, including 33 as first or corresponding author in high-impact journals such as *Sci. Adv.*, *Nat. Commun.*, *J. Am. Chem. Soc.*, and *Angew. Chem. Int. Ed.* She has also applied for and been granted 10 invention patents.

Currently, she serves as:

- Associate Editor of *Colloids and Surfaces A: Physicochemical and Engineering Aspects*;
- Editorial Board Member of *Frontiers in Chemistry*;
- Member of the Youth Committee of the Colloid and Interface Chemistry Division, Chinese Chemical Society.

**Song Liu**

Song Liu is a Professor at Northeast Forestry University. He received his B.S. degree in 2014 from Jilin University and his Ph.D. in Catalysis in 2020 from the Dalian Institute of Chemical Physics, Chinese Academy of Sciences. His research interests include the design and preparation of efficient biomass-based electrocatalytic materials, mechanism analysis of electrocatalytic reactions, and electrocatalytic biomass conversion.